



LAWRENCE
LIVERMORE
NATIONAL
LABORATORY

The Role of Pore Geometry in Single Nanoparticle Detection

M. Davenport, K. Healy, M. Pevarnik, N. Teslich, S.
Cabrini, A. P. Morrison, Z. S. Siwy, S. E. Letant

July 13, 2012

ACS Nano

Disclaimer

This document was prepared as an account of work sponsored by an agency of the United States government. Neither the United States government nor Lawrence Livermore National Security, LLC, nor any of their employees makes any warranty, expressed or implied, or assumes any legal liability or responsibility for the accuracy, completeness, or usefulness of any information, apparatus, product, or process disclosed, or represents that its use would not infringe privately owned rights. Reference herein to any specific commercial product, process, or service by trade name, trademark, manufacturer, or otherwise does not necessarily constitute or imply its endorsement, recommendation, or favoring by the United States government or Lawrence Livermore National Security, LLC. The views and opinions of authors expressed herein do not necessarily state or reflect those of the United States government or Lawrence Livermore National Security, LLC, and shall not be used for advertising or product endorsement purposes.

The Role of Pore Geometry in Single Nanoparticle Detection

Matthew Davenport^{1,2}, Ken Healy^{2,3}, Matthew Pevarnik², Nick Teslich¹, Stefano Cabrini⁴, Alan P. Morrison³, Zuzanna S. Siwy² and Sonia E. Létant¹

¹ Physical and Life Sciences, Lawrence Livermore National Laboratory, 7000 East Ave. Livermore, CA 94550

² Department of Physics and Astronomy, University of California, Irvine, 4129H Frederick Reines Hall Irvine, CA 92697-4575

³ Department of Electrical and Electronic Engineering, University College Cork, Ireland

⁴ Molecular Foundry, Lawrence Berkeley National Laboratory, 1 Cyclotron Rd., Berkeley, California 94720

Abstract

In this report, we observe single nanoparticle translocation events via resistive pulse sensing using silicon nitride pores described by a range of lengths and diameters. Pores are prepared by focused ion beam milling in 50 nm-, 100 nm- and 500nm-thick silicon nitride membranes with diameters fabricated to accommodate spherical silica nanoparticles with sizes chosen to mimic that of virus particles. In this manner, we are able to characterize the role of pore geometry in three key components of the detection scheme, namely event magnitude, event duration and event frequency. In all three aspects, we find that the electric field created by the applied voltage and the pore's geometry is a critical factor. We develop approximations to describe this field – which are verified with computer simulations – and interactions between particles and this field. For the first time, we are able to mathematically account for the insignificant change in a pore's access resistance due to translocating particles to better predict event magnitudes. These approximations also provide a suitable foundation for estimating the zeta potential of the particles and/or pore surface when studied in conjunction with event durations. We also verify that translocation achieved by electro-osmotic transport is an effective means of slowing translocation velocities of highly charged particles without compromising particle capture rate as compared to more traditional approaches based on electrophoretic transport. These approximations and observations could enable the optimization of single pore devices and potentially networked architectures utilizing multiple pore geometries to detect specific targets or unknown analytes.

Single particle detection techniques based on driving nanoparticles through submicron or nanoscopic pores with a voltage or pressure gradient have been the subject of numerous studies over the past two decades.¹ This, in large part, is due to the potential of nanopore-based platforms to differentiate between base pairs of nucleic acid chains as the molecule threads through the pore, which could provide a low-cost, high-throughput means of DNA sequencing.²⁻¹⁰ However, the history of pore-based detection schemes starts much earlier – nearly 60 years ago - with the counting of blood cells as they passed through a microscopic hole in a glass tube.¹¹ Based on the same principles, these recent strides towards DNA sequencing are a result of key advancements in the interim.

In the context of solid-state nanopores, the key advancements were technological in nature; micro- and nanofabrication techniques were developed to allow for the production of smaller holes to address smaller and more fundamental biological particles, such as the aforementioned DNA, but also including RNA and proteins.^{6,12-13} Between microscopic cells and their nanoscopic building blocks, however, exist a class of particles as important biologically as they are to the development of pore-based particle detection: viruses, which range from roughly 20 nm to upwards of 600 nm. Scale is perhaps the most important consideration in the pore sensing technique. Current carrying ions in the background electrolyte are temporarily excluded from the pore as the particle moves through it, or translocates, as shown in Scheme 1. The magnitude of this change, or event, along with its duration provides information regarding the particle's size and surface chemistry. Conversely, if the particle is well characterized in terms of size and chemistry, one can study how variations in the pore's properties influence particle translocation and the transduction thereof.¹⁴⁻¹⁵ In this report, we focus on the theme of scale to investigate how a pore's length and diameter affect the shape of the event, along with the nature of the transport mechanisms that drive translocation.

Studies conducted over the past several years provide a wealth of information on this front, but the data tends to accumulate in one of two extremes which can be understood in terms of the pore

aspect ratio, that is its length divided by its diameter. Early (*circa* 1970) studies focused on high-aspect ratio pores, which could be considered long and narrow with lengths orders of magnitude larger than the particle being detected.^{14,16-17} That is not to say that more recent publications do not also use these types of pores, but more modern fabrication techniques are allowing for smaller pore diameters and even higher aspect ratios, which are able to more intimately probe particles.¹⁸⁻²³ These glass and polymeric pore materials present a set of challenges: there is no straightforward manner in which to reduce the thickness of the membrane, and thus pore length, to less than $\sim 1 \mu\text{m}$ or in which to integrate these nanopores into microelectromechanical systems (MEMS) to enable high-throughput, small volume lab-on-a-chip-type device architectures. These challenges have lead researchers to probe different materials and a new extreme.

Silicon nitride pores are amenable to a wide range of fabrication techniques- the choice is generally guided by the size of the target analyte - and are easily integrated with commonly used microfluidic systems. They can be deposited in a wide range of thicknesses, from nm to μm , which has allowed researchers to investigate virion-sized particles with low to ultra-low aspect ratio pores.²⁴⁻²⁶ There are studies in the intermediate aspect ratio regime utilizing other solid-state devices, but these examine single pore geometries and tend to rely on the same analysis as high aspect ratio pores.²⁷⁻³¹ For this reason, we wanted to examine a range of pore lengths and diameters to bridge these gaps in both data and understanding.

Results and Discussion

To build upon the framework of earlier studies, we examine a range of silicon nitride membrane thicknesses (L) and pore diameters (D) as shown in Figure 1. To test their response to a range of particle sizes, silica nanoparticles defined by two distinct size distributions, with mean particle diameters (d) of 57 nm and 101 nm, were chosen to highlight a subset of virion sizes (see Figure 2e). For the

purposes of this text, though, we will use the nominal diameters as supplied by the vendor for distinction, *i.e.* 50 nm and 100 nm. In the context of resistive pulse sensing, this examination of response involves identifying the probability distribution functions, or PDFs, that best describe the event depths and event durations, extracting the parameters that define these distributions and assessing how these parameters vary with pore geometry, particle size and applied voltage. Over the course of developing and discussing the significance of these PDFs in relation to these parameters, several variables will be introduced, so we present Table 1 as a quick reference guide for our notation.

Table 1: Variable Definitions

Variable	Definition	Variable	Definition	Variable	Definition
D	Pore Diameter	I_o	Open Ionic Current	v_{mp}	Most Probable Translocation Velocity
L	Pore Length	I_b	Blocked Ionic Current	r	Radial Distance from Pore Mouth
d	Particle Diameter	i	Event depth; $(I_o - I_b)/I_o$	v_{EP}	Electrophoretic Velocity for $r \leq D$
U	Applied Electric Potential Difference	i_{mp}	Most Probable Event Depth	v_{EO}	Electro-osmotic Velocity for $r \leq D$
R	Total Pore Resistance	Δt	Event Duration	v	Particle Velocity for $r > D$
R_p	Geometric Resistance	Δt_{mp}	Most Probable Event Duration	E_z	Electric field for $r \leq D$
R_a	Access Resistance	τ	Event Duration Time Constant	E_{cis}	Electric Field for $r > D$
α	R_a/R_p	τ	Time Between Events	ζ_{pore}	Pore Zeta Potential
β	Field Interaction Coefficient	f	Event Frequency	$\zeta_{particle}$	Particle Zeta Potential
χ	Pore Volume Excluded by Particle	ξ	Event Frequency Scaling Factor	δ	Diffusion Coefficient

In the event that a variable is subscripted with a number, it is understood that the number indicates the dimension used to identify the object, *e.g.* L_{50} = 50 nm long pore and d_{100} = 100 nm diameter particle. When zeta potentials and diffusion coefficients are subscripted with “d50” or “d100”, it is understood to reference the value for 50 or 100 nm particles, respectively. For example, ζ_{d50} would be the zeta potential of 50 nm particles and δ_{d100} is the diffusion coefficient for 100 nm particles.

Event Depth

Depending on the report, event depths may be reported in terms of the magnitude of the change in pore resistance, R, from an unobstructed, open state to a blocked state (subscripted with an “o” or “b” respectively), $\Delta R = |R_o - R_b|$, or the change in ionic current, $\Delta I = |I_o - I_b|$. Of course, this blockage is caused by the translocating particle. Frequently, these quantities are presented relative to their values measured in the absence of particles, $\Delta R/R_o$ or $\Delta I/I_o$. Because our pores impede ionic

current in an entirely ohmic fashion, resistance and current can be used interchangeably with the appropriate application of Ohm's law:

$$(1) U = IR$$

where U is the applied electric potential difference across the membrane. Since I and U are continuously monitored by the patch-clamp amplifier during bead translocation, it is straightforward to evaluate the quantity of our choosing and we have found each to be useful in interpreting our results.

Understanding the pore resistance is crucial as it immediately relates a pore's geometry to the behavior of the system. Let R represents the sum of all the resistive elements impeding current. For our pores, R represents the sum of the series combination of the pore's geometric resistance, R_p , and its access resistance, R_a . Our pores are, to first order, cylindrical, allowing us to write

$$(2) R_p = \frac{4L}{\pi\kappa D^2}$$

where κ is the conductivity of the electrolyte. R_a is the resistance created by ions converging to a small aperture from a semi-infinite reservoir.³²

$$(3) R_a = 2 \times \frac{1}{2\kappa D} = \frac{1}{\kappa D}$$

The factor of two comes from both the pore entrance and exit contributing to the overall access resistance. The total resistance is then given by summing Eqs. 2 and 3:

$$(4) R = R_p + R_a = \frac{4L + \pi D}{\pi\kappa D^2}$$

establishing the relationship between the current established by applying a voltage and pore geometry.

However, we chose to present our results primarily as $\Delta I/I_0$ to emphasize that, in every device, current is being measured and the division by the baseline current value allows for a more direct comparison of pores over the variables considered. To simplify notation, we introduce $i = \Delta I/I_0$ to indicate the event depth as a current relative to its baseline value, reported as a percentage. As the probability distribution associated with event depths is Gaussian, the relevant parameters are the most probable event depth, i_{mp} , and the variance, σ_i^2 (or simply σ_i , the standard deviation).

$$(5) P(i) = Ce^{-\frac{(i-i_{mp})^2}{\sigma_i^2}}$$

with C being a constant of normalization.

Figure 2 shows histograms and corresponding Gaussian curves and fit parameters for three pores of similar diameters fabricated in three membrane thicknesses. We observe large values of σ_i relative to the mean event depth values, which is easily understood considering the particle size distributions. Given that the i histograms also capture the shape of the particle size histograms - skewed slightly to higher values for the 50 nm particles and slightly towards lower values for the 100 nm particles – and that peaks are narrower for d_{50} particles versus d_{100} particles, we are confident that it is the variation in particle diameter versus pore diameter which dominates the shape of the curve. Therefore, we assume that inhomogeneities in the manner in which the particles translocate the pore do not influence to the PDF's shape, *e.g.* differences which could be attributed to particles that travel along the pore's central axis versus those that do not are negligible. In this light, larger σ_i values are favorable as they suggest a heightened sensitivity to particles of a different size; however, since the particle size distribution is continuous, the size resolution of the devices cannot be determined.

Another striking feature of the histograms is that they suggest that working with the shortest pore does not guarantee the largest relative change in current. In the context of the previous discussion of the resistive pulse mechanism, which is based on the particle excluding current carrying ions from the pore's volume during translocation, this result is somewhat surprising: for a given ratio of particle diameter to pore diameter, decreasing the pore length decreases the fraction of the pore's volume occupied by current carrying ions, which would seemingly result in greater values of i_{mp} . However, one set of histograms does not constitute a trend, so to present the mean values of i_{mp} over the range of pore geometries studied, we introduce χ , the ratio of the pore's volume occupied by a particle to the total pore volume:

$$(6) \quad \chi = \begin{cases} \frac{2d^2}{3D^2}, & d > L \\ \frac{2d^3}{3LD^2}, & d \leq L \end{cases}$$

The most probable event depth is plotted against χ in Figure 3a-3c as unfilled points. The linearity of these plots implies that the event depth is intimately tied to the excluded volume and supports the recent report that this simple consideration alone can be useful for approximating i_{mp} in 50 nm membranes.²⁵ It is also worth noting that the slope value increases with increasing pore length, supporting the claim that shorter pores do not necessarily result in the largest changes in current. However, the fact that there is this variation indicates that the excluded volume alone is insufficient to fully characterize i_{mp} , especially in terms of the pore length.

Though there exist rigorous theoretical treatments to explain the event depth in terms of pore dimensions, the nature of the problem requires that assumptions be made, such as $D \ll L$ or $d \ll D$, to reach an analytical solution.¹⁶ While our systems clearly violate these assumptions, these previous treatments have enabled us to develop an empirical model consistent with our findings.

Recall that the pore's resistance dictates the magnitude of the ionic current in response to an applied voltage and this resistance is the sum of the pore's geometrical and access resistance. Recent work by Tsutsui et al using microscale pore diameters in 50 and 400 nm-thick membranes suggests that the access resistance is largely unaffected during particle translocation.²⁴ To further investigate this hypothesis, we turned to the resistive pulse analysis of DeBlois and Wesley, who introduced a parameter α to compensate for external resistances, R_{ext} , which are resistances in the system not stemming from the pore.¹⁷

$$(7) \quad \alpha = \frac{R_{ext}}{R}$$

In the limit that the access resistance is completely unaffected by the particles, it can be treated independently of the pore's geometric resistance, essentially behaving as an external resistance. Thus,

$$(8) \quad \alpha = \frac{R_a}{R_p} = \frac{\pi D}{4L}$$

To complete our assessment, we include the coefficient β to address the distinct cases of whether the particle's diameter is larger or smaller than the length of the pore. Briefly, this factor accounts for the distortion of the electric field lines inside the pore created by the presence of a particle. As such, it is a function of both the pore and particle geometries. For a more complete discussion of this effect, we refer the reader to the works of DeBlois and Bean and also Gregg and Steidley, from which we have gleaned the following values:^{16,33}

$$(9) \beta = \begin{cases} 1, & d \geq L \\ \frac{3}{2}, & d < L \end{cases}$$

It is unlikely that β is discontinuous in this fashion; however, determining precise values would require numerical simulations and we have found that the straightforward approximation of Eq. 9 is sufficient to describe our results.

Based on these considerations, we can express i_{mp} in terms of the geometries of the pores and particles as:

$$(10) i_{mp} \approx \frac{\beta\chi}{1+\alpha} = \begin{cases} \frac{d^3}{\left(L + \frac{\pi D}{4}\right) D^2}, & d < L \\ \frac{2d^3}{3\left(L + \frac{\pi D}{4}\right) D^2}, & d = L \\ \frac{2Ld^2}{3\left(L + \frac{\pi D}{4}\right) D^2}, & d > L \end{cases}$$

We again plot the mean event depths, but with the abscissa values being given by $\beta\chi/(1+\alpha)$, shown as filled points Figure 3a-3c. With the values of the slope being consistent across the membrane thicknesses and very nearly unity, we believe we have captured the most relevant parameters in describing the ionic current through a pore device in response to translocating particles. We would like to point out that the formulation for $d < L$ agrees with that proposed by Sun and Crooks for micron-long carbon nanotube-based Coulter counters.²³

While the results shown in Figure 3 clearly support the hypothesis of invariant access resistance during particle translocation proposed by Tsutsui *et al* and suggest that this is a relevant concern in even

longer pores, we caution the reader not to place too much emphasis on the length itself.²⁴ Rather, the inclusion of $(1+\alpha)^{-1}$ demonstrates the pore's aspect ratio is the more relevant parameter. That the access resistance is largely unaffected by particle translocations also suggests that interactions near and inside the pore itself are responsible for determining even depth. As will be shown, these interactions are mediated by the electric field in the vicinity of the pore, which is also intimately related to a pore's aspect ratio.

Event Duration

As discussed previously, the resistive pulse detection scheme relies on the characterization of translocation events by their intensity and duration. While the event depth affords insight into a particle's size relative to the pore, studying the event duration can provide information on a particle's charge. Chemically distinct particles of the same size cannot be distinguished solely by event depth analysis; however, if these unique chemistries result in differences in surface charge, event duration can provide distinction where event depth cannot. Particles possessing higher charge will have stronger interactions with an applied electric field, meaning their translocation velocities will differ from particles of lower charge and will be measured as different event durations. These differences can be then used to determine the magnitude of the surface charge.²⁹ Furthermore, the distribution of translocation times can be used to reveal the nature of interactions between the analyte and the pore itself.³⁴

Recently, Bacri *et al* used this approach to identify three distinct types of events for silica nanoparticles of a single size translocating 180 nm diameter pores in 50 nm thick silicon nitride membranes: short, medium and long events.²⁵ The first case is attributed to particle collisions with the pore, that is, a particle approaches the pore but does not completely translocate through it. Long events are interpreted as one particle entering the pore as another exits, meaning they are essentially

observing two successive events with no resolvable temporal separation. Finally, the medium-duration events are indicative of traditional translocation. In our experiments, all three behaviors were observed but only “normal” translocation events (*i.e.*, single particles, medium-event duration) were included for analysis. Collision-type events could be easily identified, and thus neglected, by their shallow depths. As we operated at lower voltages compared to the Bacri et al report, the long-type events were rare and were usually followed by particles “sticking” inside the pore. Stuck particles could frequently be ejected by reversing the polarity of the applied electric potential; however, every translocation experiment does ultimately end with a particle irreversibly clogging the pore.

This clogging problem is not unique to our pores and is indeed the subject of ongoing research.³⁵ Generally speaking, the approach adopted to combat this fouling in silicon nitride pores is to functionalize the surface through chemical modifications. We elected an easier, lower-cost alternative in this study, involving the enhancement of the negative surface charge of both the pore and particles by simply working at an elevated pH value of 10 to strengthen the electrostatic repulsion between the two. Silicon nitride’s surface chemistry is quite similar to silicon oxide: for thin films, it has been shown that upwards of 98% of the surface groups are silanes.³⁶ At pH 10, we expect the large majority of these groups to be deprotonated. A somewhat surprising consequence of this elevated surface charge is the resulting electro-osmotic (EO) flow through the pore is sufficient to transport particles and virtually eliminate electrophoretic (EP) translocation, which is typically employed in pore sensing platforms. Scheme 2 is presented to help visualize the electrokinetics of our system: The EP component of a particle’s motion is the response of the charged particle to the applied field. Because our particles are negatively charged, their EP motion will be antiparallel to the electric field. Electro-osmosis is the motion of the solvent coupled to the ionic motion. The pore’s negative surface charge enhances the cation concentration inside the pore, thus when a field is applied, their motion generates fluid flow

parallel to the applied field. For a more detailed discussion on the electrokinetics in nanopores, the reader is referred to the work of Schoch *et al.*³⁷

Having a qualitative understanding of the interactions responsible for the particle's motion, we now turn to a more focused analysis of our data to explore what information can be gained to develop a more quantitative description. In the presence of a field, the resulting electrokinetic velocity components can be expressed in the following way:

$$(11) \mathbf{v}_{EP} = \frac{\epsilon}{\eta} \zeta_{\text{particle}} \mathbf{E}$$

$$(12) \mathbf{v}_{EO} = -\frac{\epsilon}{\eta} \zeta_{\text{pore}} \mathbf{E}$$

Summing Eqs. 8 and 9 will give the resultant velocity vector:

$$(13) \mathbf{v} = \mathbf{v}_{EP} + \mathbf{v}_{EO} = \frac{\epsilon}{\eta} (\zeta_{\text{particle}} - \zeta_{\text{pore}}) \mathbf{E}$$

where v is the velocity, ϵ is the product of the permittivity of free-space and the dielectric constant of water (the solvent), η is the viscosity of water, ζ represents the zeta potential of the pore or particle (note the subscripts), and E is magnitude of the electric field (boldfaced variables represent vector quantities).³⁷ Briefly, the zeta potential is the electrostatic potential at the boundary between the immobile counterions surrounding a charged surface and the freely diffusing bulk phase. Thus, it is intimately related to the surface charge and ionic strength of the electrolyte, but provides a more convenient quantity to work with as the zeta potential of the nanoparticles can be readily measured using electrophoretic light scattering (or ELS, see *Methods* section).

As suggested by Scheme 2, we will assume that the velocity is solely in the +z-direction (from the *cis* chamber to the *trans* side of the membrane). Zeta potentials were found to be $\zeta_{d50} = -26.0 \pm 3.0$ mV and $\zeta_{d100} = -33.9 \pm 3.0$ mV for the 50 and 100 nm particles, respectively. Combining an expression developed by Yusko *et al* with the zeta potential found for silicon nitride at pH 10 in 400 mM KCl in the Firnkes's report, we can estimate the zeta potential of the pore in 100 mM KCl at pH 10, which was found to be -

44.0 mV.³⁸⁻³⁹ We rewrite Eq. 10 to emphasize EO dominates EP and that we have reduced the problem to one dimension:

$$(14) v_z = \frac{\epsilon}{\eta} (|\zeta_{\text{pore}}| - |\zeta_{\text{particle}}|) E_z$$

We are now left only to determine expressions for the particle velocity and the electric field in the z-direction, v_z and E_z respectively.

Despite the heightened nanopore surface charge, we do not believe the resulting static electric field strongly influences the translocation times and its primary role is to frustrate silica particles from clogging the pore should they approach its surface. Counterions present in the electrolyte screen this surface charge over the Debye length, which is on the order of 1 nm in 100 mM KCl (the electrolyte used in our experiments). Therefore, the only electric field that bears consideration – in terms of Eq. 14 - will be a consequence of the applied voltage. Since the driving force in and around the pore will be closely related to the voltage drop across the pore's length, or U_p , U_p/L seems a reasonable approximation. Using finite element simulations, we were able to verify that this is in fact a reasonable estimate; however, it is important to mention that this approximation neglects significant edge effects and radial variations of the field within the pore as shown in Figure 4.

Turning to the particle velocity, we present Figure 5 as an example of the duration distributions for translocation times, or Δt , for the three pore thicknesses at $U = +150$ mV. The distribution of Δt values corresponds to a distribution of particle velocities, but it is immediately evident from the shape of the plots that there is a most probable translocation time, Δt_{mp} , and, hence, a most probable velocity, v_{mp} . Note that for durations greater than the most probable translocation time ($\Delta t > \Delta t_{\text{mp}}$), the distribution decays in an exponential fashion. For this reason, we have defined τ as a time-constant-like parameter such that the probability of an event having $\Delta t = \Delta t_{\text{mp}} + \tau$ is equal to the probability at Δt_{mp} divided by e , the base of the natural logarithm.

The following analysis is nearly identical to that used in the previous section: we are once more interested in the PDF that best describes our distributions such that we can determine the parameters Δt_{mp} and τ . As the distribution clearly involves an exponential decay, we restrict our search to functions from the exponential family. We chose to focus on two for this study: the lognormal distribution (LN) and the inverse Gaussian distribution (IG):

$$(15) P_{LN}(\Delta t) = \frac{C_1}{\Delta t \sigma \sqrt{2\pi}} e^{-\frac{(\ln \Delta t - a_1)^2}{2s_1^2}}$$

$$(16) P_{IG}(\Delta t) = C_2 \sqrt{\frac{s_2}{2\pi \Delta t^3}} e^{-\frac{\lambda(\Delta t - a_2)^2}{2\Delta t s_2^2}}$$

where the C values are constants related to the total number of counts for a given experiment, the a values are related to the mean of the distribution and the s parameters are tied to the shape of their respective PDFs. Once these parameters are identified, the derivative of the PDFs can be taken to identify the point at which they reach their maxima - Δt_{mp} - and the point at which they decay to $1/e$ of their maxima - $\Delta t_{mp} + \tau$.

Before finalizing the velocity analysis, let us briefly comment on the PDFs themselves. When the logarithm of the variable of interest - in this case, the translocation time - is distributed according to a Gaussian or normal distribution, the variable itself is lognormally distributed. Event durations for carbon nanotubes and nucleosomal substructures moving through nanopores have been shown to be described well by LN distributions.⁴⁰⁻⁴¹ For the former, it was suggested that this distribution was also related to the length distribution of the nanotubes. By inspection (refer to Figure 2d), a similar argument could be made for the d_{50} particles used in our experiments, but clearly breaks down when applied to the d_{100} particles. The IG distribution is known to describe the motion of particles under the influence of a force introducing a drift component in the same direction as the net diffusive motion (distributions were identified independently by Schrödinger and Smoluchowski in 1915, although these were not formalized until decades later).⁴² Both PDFs were found to characterize the shape of our

distributions well and since neither one “outperformed” the other in terms of statistical significance tests (see *Methods* section), the Δt_{mp} and τ resulting from the LN and IG fits were averaged.

The most probable translocation time allows us to define the most probable translocation velocity:

$$(17) v_z = v_{mp} = \Delta z / \Delta t_{mp}$$

where Δz is the distance the particle travels during the event. Simulations performed by Prabhu et al have found that the ionic current begins to fall from its baseline value, or that the translocation event starts, when the particle is approximately one pore diameter away from the pore mouth.²⁶ By symmetry, then, the event concludes once the particle is a pore diameter away from the pore exit.

Thus, $\Delta z = 2D + L + d$, and substituting into Eq. 15 gives:

$$(18) v_{mp} = (2D + L + d) / \Delta t_{mp}$$

Interestingly, from our simulations, we note that the magnitude of the z-component of the electric field drops to 10% of its maximum value within roughly one pore diameter away from the pore mouth. Supporting what we saw in the event depth analysis, this implies that it is only interactions that take place within the neighborhood of the pore (defined by D) that are significant in resistive pulse sensing, which is another way of stating the voltage drop across the access resistance is not significantly affected by the particles.

We can now write the most probable velocity in terms of measurable quantities, but the question remains as to the role of τ . Similar to the σ_i value of the event depth histograms, τ gives an idea of the width of the duration distribution. However, an important difference between σ_i and τ is that the Δt distribution is always skewed towards higher values; that is, the shape of the distribution does not reflect that of the particle sizes and furthermore, as shown in Figure 5d, τ does not appear to be influenced by the field or pore geometry. This would suggest that the particle size distribution is not responsible for variations in τ and larger τ values may be due to increased interactions with the pore

(such as sticking) or a broad distribution of particle zeta potentials. This is compounded by the fact that zeta potentials of silicon nitride surfaces have been observed to vary over time.^{36, 38} Ultimately, this means that $(|\zeta_{\text{pore}}| - |\zeta_{\text{particle}}|)$ is difficult to define by a single value in our system and in order to simplify further analysis to cases with the smallest range of $(|\zeta_{\text{pore}}| - |\zeta_{\text{particle}}|)$, we ignore experiments characterized by large τ , or $\tau > 0.6$ ms. While this value is arbitrary, it does distinguish what we interpret to be a class of experiments characterized by narrow zeta distributions and/or minimal particle-pore interactions from those which are not (see Figure 5d).

While we expected a monotonic increase of v_{mp} with E_z , that is not the case as shown in Figure 6 where v_{mp} is averaged over 0.1 mV/nm intervals in E_z for each membrane thickness. However, that is not to say nothing valuable came of this analysis. Clearly, 50 nm particles translocate significantly faster than 100 nm particles, demonstrating that electro-osmotic transport can be utilized as an effective means of slowing the translocation of highly charged particles. Furthermore, the large number of experiments performed allows for the determination of average ζ values; for a pore-based device, however, one would want to achieve reliable results with minimal runs.

Nonetheless, using Eq. 11 to calculate ζ_{pore} treating the ζ_{particle} values as known quantities, we find an average value of $\zeta_{\text{pore}} = -42 \pm 8$ mV. While this is in excellent agreement with the estimation of ζ_{pore} presented earlier in this section (*i.e.*, $\zeta_{\text{pore}} = -44$ mV), the uncertainty is quite large, which is reflective of the wide range of velocities measured at similar E_z values, even with the $\tau > 0.6$ ms restriction employed, which can be seen in the error bars of the charts presented in Figure 6. If we assume ζ_{pore} is fixed at -44 mV to calculate ζ_{particle} , we find values consistent with independent measurements: $\zeta_{\text{d50}} = -31 \pm 6$ mV and $\zeta_{\text{d100}} = -34 \pm 8$ mV, compared to $\zeta_{\text{d50}} = -26 \pm 3$ mV and $\zeta_{\text{d100}} = -34 \pm 3$ mV from ELS.

Bead Mixtures

As the reader may have already noted, each histogram has been shown for one bead size measured separately from the other thus far. While these histograms clearly imply that a single pore should be able to differentiate silica particles based on their size, it is essential to verify this implication: for a nanopore sensor to accurately identify the size and geometry of an unknown particle, a known “standard” particle whose diameter is equal to the length of the membrane should be included in the suspension to identify the β value for the unknown particle. In the absence of standard particle, it may be possible to accurately address unknown particles by incorporating multiple single-pore membranes into the same detector and analyzing the event characteristics from each individual pore; however, our current experimental set-up does not yet allow for this configuration. Figure 7 shows scatter plots for suspensions containing a mixture of 50 nm and 100 nm particles in each membrane thickness at comparable E_z values, flanked by the histograms for event depth and event duration. Bead mixtures present an additional challenge in that one must acquire N times more events compared to a monodisperse sample, where N is the number of different bead sizes present in the same sample (assuming that the total bead concentration is roughly equivalent), to build a statistically meaningful histogram for all N species.

As an example of this, compare the event duration histograms for the L_{500} pore to the L_{50} and L_{100} pores. In the latter two cases, one can discern two peaks, whereas only one appears in the L_{500} pore. By sorting events according to event depth, we can break the event duration histograms into two distributions – both of which are described by lognormal and inverse Gaussians as described in the previous section as shown in the light purple insets of Figure 7. From this analysis, we can see that there are indeed two separate Δt_{mp} values for the 500-nm long pore as well, yet the relatively low count number for the smaller beads make these indistinguishable when the mixture is viewed as a whole. The fact that we can utilize this post-processing technique based on event depth certainly minimizes this concern as we are still able to obtain the parameters of interest from the PDF fittings.

Returning to the earlier idea of a “standard” particle size, we can test this notion by assuming one of the particle sizes is known and using it to calculate the size of the other particle. As a pivotal role of the standard would be to provide an estimate for which β to use for the unknown particle, the particle whose diameter is closest to the membrane thickness is treated as the standard. The results of this exercise are shown in Table 2 and the agreement is, generally speaking, quite good as all but one of the d_u values fall within one standard deviation of the mean obtained from SEM sizing (refer to Figure 2d). Recall that the values of β were obtained from studies which examined cases where $L \gg d$ or $L \leq d$, thus it is not altogether surprising that our intermediate case of the L_{500} pore deviates the most. However, it is worth noting that this deviation is less than 5 nm outside one standard deviation from the mean particle size determined for the d_{50} particles by SEM (which was 57 ± 11 nm). Similarly, treating the zeta potential measured with ELS for the standard particle as a known quantity, we are able to determine values for the zeta potential of the pore and unknown particle which are consistent with values measured in the previous section, with all the ζ_u values falling within the uncertainty measured earlier and all but the 202 nm diameter, 50 nm long pore returning ζ_{pore} values within the range determined previously.

Table 2: Using Nanopores as “Unknown” Particle Analyzers

L (nm)	D (nm)	d_s (nm)	β_u	d_u (nm)	ζ_s (mv)	ζ_{pore} (mv)	ζ_u (mv)
50	202	57	1	104 ± 10	-26	-32 ± 4	-29 ± 4
50	252	57	1	92 ± 2	-26	-34 ± 2	-30 ± 1
50	328	57	1	111 ± 6	-26	-38 ± 3	-32 ± 2
100	224	101	3/2	56 ± 1	-34	-41 ± 3	-31 ± 3
100	226	101	3/2	60 ± 3	-34	-40 ± 1	-31 ± 1
100	234	101	3/2	55 ± 1	-34	-39 ± 2	-29 ± 1
500	307	101	3/2	71 ± 3	-34	-49 ± 2	-26 ± 1

Results from treating one particle’s diameter and zeta potential as a known standard, d_s and ζ_s , respectively, and using these to calculate “unknown” properties of the system, which are subscripted with a “u” in the table. By using the particle with the diameter closest to the

membrane thickness, we can identify whether the unknown bead is larger or smaller than the membrane and use the appropriate β and form of Eq. 11 to obtain d_u . Eq 14 can be used with ζ_s to calculate ζ_{pore} , which can then be used to determine ζ_u .

Capture Rates

The rate at which events occur, or the capture rate, is also a critical consideration. This will determine how long an experiment must be run in order to record enough events to record meaningful statistics (typically several hundred). To determine the capture rates in each of our experiments, the time between successive events, T , is tracked and the resulting distribution is plotted as shown below in Figure 8. When the particles do not interact with one another, these distributions can be fit with an exponential decay of the form:

$$(19) P(T) = Ce^{-fT}$$

where f is the capture rate and C is a constant such that $\int_0^{T_{\text{max}}} P(T) dT = n$, the total number of events in a given experiment. The three rates expressed in Figure 8 are fairly representative of all experiments; that is, event frequencies were on the order of 1 – 10 Hz. Taking the bead concentration into consideration (10^9 - 5×10^{10} particles/ml), this is nearly identical to capture rates reported for electrophoretic nanoparticle translocation. As particle concentration increases, so does the event frequency. Bacri et al measured rates that were 10-100 times higher than ours with silica particles in thin silicon nitride pores with ~ 100 times higher bead concentration.²⁵ Similarly, observing polystyrene beads translocations in a CNT based apparatus, Sun and Crooks were able to capture up to 20 polystyrene particles/s using a concentration of 5×10^{11} particles/ml.²⁸

In addition to the concentration, the rate at which particles are delivered to the pore, which is controlled by their electric field driven motion, will also influence event frequency. We again encounter the important distinction of scale in our system: in the event depth and event duration sections, we found that only interactions in the immediate vicinity of the pore (*i.e.*, within one pore diameter) played

an important role; however, the rate at which particles enter this region will be controlled by the field outside of it. Wanunu *et al* and Wong and Muthukumar developed analytical expressions for this rate in the cases of pure electrophoresis and electro-osmosis, respectively, which we can combine to develop a more complete treatment for the electrokinetics outside the pore, and ultimately the capture rate.⁴³⁻⁴⁴

Central to both studies is the concept of a capture radius. A particle is said to have entered the capture radius of the pore once its random diffusive velocity is overcome by directed, field-driven motion. Letting r represent the radial distance from the center of the pore, we choose to write velocities for $r > D$ as v rather than v to avoid confusion. We also assume solvent and current flow is in the radial direction alone.

The electroosmotic component of this motion, $v_{EO}(r)$, is a result of the continuity of fluid flow: the fluid flux into the pore must be equal to the flux out of the pore.

$$(20) v_{EO}(r) = \frac{A_{pore} v_{EO}}{2\pi r^2} = \frac{\epsilon |\zeta_{pore}| VD^2}{8\eta(L + \frac{\pi D}{4})r^2}$$

where A_{pore} is the cross-sectional area of the pore. Just as before, the electrophoretic component, $v_{EP}(r)$, is simply the motion resulting from the field acting on the charge of the particle; however, we must remain aware that this is the field outside of the pore, which we will call E_{cis} .

$$(21) E_{cis}(r) = -\frac{\partial U_{cis}}{\partial r} = \frac{I \partial R_{cis}}{\partial r} = \frac{\pi \kappa UD^2}{4L + \pi D} \left(\frac{\partial R_{cis}}{\partial r} \right) = \frac{\pi \kappa UD^2}{4L + \pi D} \left(\frac{\partial r}{2\pi \kappa r^2 \partial r} \right) = \frac{UD^2}{2(4L + \pi D)r^2}$$

The above utilizes the resistance of a vanishingly thin hemispherical shell, $\partial R = \frac{\partial r}{2\pi \kappa r^2}$, and the fact that the direction of current flow is opposite of ∂r , accounting for the disappearance of the negative sign with the introduction of I .

$$(22) v_{EP}(r) = -|\zeta_{particle}| E_{cis}(r) = -\frac{\epsilon |\zeta_{particle}| UD^2}{2\eta(4L + \pi D)r^2}$$

Rounding out the pertinent velocities is the diffusive velocity of particle on the length scale r , which is given by:

$$(23) v_{\text{dif}}(r) = \frac{\delta}{r}$$

where δ is the particle's diffusion coefficient. At the capture radius, r^* :

$$(24) v_{\text{EO}}(r^*) + v_{\text{EP}}(r^*) = \frac{\delta}{r^*}$$

Substituting and solving for r^* gives:

$$(25) r^* = \frac{\epsilon U D^2}{2\eta\delta(4L + \pi D)} \left(|\zeta_{\text{pore}}| - |\zeta_{\text{particle}}| \right)$$

For a perfectly absorbing hemisphere of radius r^* , the capture rate is:

$$(26) f = 2\pi N_c \delta r^* = \frac{\pi N_c \epsilon U D^2}{\eta(4L + \pi D)} \left(|\zeta_{\text{pore}}| - |\zeta_{\text{particle}}| \right)$$

with N_c being the number of particles per cubic meter. To simplify notation, we let $\xi = \frac{\pi N_c \epsilon U D^2}{\eta(4L + \pi D)}$. While this simplification could be achieved by expressing the right-most side of the equation in terms of E_z or even v_z from the previous section, we intentionally present it in this manner to again stress that it is a result of considering interactions that take place outside the pore vicinity. Indeed, as we show in Figure 9d, the capture radius can be more than an order of magnitude larger than the pore diameter.

Based on Eq. 26, it once again appears that the quantity of interest will depend on the difference between the zeta potential of the pore and that of the particles. For this reason, we employ the same restriction from the event duration analysis in which we disregard cases with broad zeta potential distributions and/or heightened non-specific pore/particle interactions (*i.e.*, when $\tau > 0.6$ ms). In Figure 9, we show the measured capture rates versus ξ , along with theoretical capture rates using the $\zeta_{\text{particles}}$ measured by ELS and ζ_{pore} calculated from Firnkes et al's data.³⁸⁻³⁹ The disagreement with theory

is not altogether unexpected considering the theoretical capture rates are approximations developed for pores of similar lengths to ours, but one to two orders of magnitude smaller in diameter. As shown from the linear fits to the experimental data, the slopes purport differences in zeta potentials within an order of magnitude in either direction. Strikingly, there do appear to be two distinct capture rates when 100 nm particles are present in the solution.

Unfortunately, in the context of these experiments we are unable to definitively comment on whether this is a consequence of a poor approximation, poorly defined zeta potentials or if something more interesting is happening in our system. Shown in Figure 10 is a trace in which both low and high capture rates are seen in the same experiment, which would suggest that one of the latter two explanations is more likely than the first. That the 100 nm particles seem to be capable of higher translocation rates than the more modestly charged 50 nm particles and that the larger particles do not fall on the lower capture rate curve for L_{100} membranes are also intriguing, but again, at present these remain curiosities. Tuning the nanopore surface potential via an embedded gate electrode, which has been discussed in recent studies, would provide an excellent route to investigate this further.⁴⁵⁻⁴⁶

Conclusions

We have presented resistive pulse analysis over a range of nanopore diameters and lengths providing more evidence that a pore's access resistance remains unaffected by translocating particles in agreement with the findings of Tsutsui et al in ultra-low aspect ratio pores.²⁵ By investigating the contribution of access resistance over this range of pore aspect ratios and building on the analysis for high aspect ratio pores, we are able to formulate an approximation for the response of the ionic current to a translocating particle which mathematically accounts for this in terms of the pore geometry relative to the particle size.

To further probe the influence of pore geometry, we studied event durations and particle capture rate as both depend heavily on the electric field that results from the applied voltage and pore

aspect ratio. We were able to develop relevant approximations for this field through an understanding of the electrokinetic transport phenomenon responsible for particle translocation, namely electro-osmosis and electrophoresis. In so doing, we demonstrated that event durations can be used as a measure of particle or pore zeta potential when electro-osmotic transport dominates and that electro-osmosis provides an effective means of driving particles through a pore and slowing the translocation velocity of heavily charged particles.

In terms of event magnitudes and durations, we have shown that the most important interactions appear to take place not just within the pore, but within a region that extends to one pore diameter to either side of the pore regardless of aspect ratio. Our capture rate analysis reveals more work is needed to identify the nature of interactions outside this region to optimize the particle capture rate, which was found to be lower and higher than anticipated and may be related to the pore aspect ratio. These findings provide valuable considerations when designing a pore sensor for a target analyte of a particular size or charge, but also illustrate how pores can be used singly or potentially networked in series or parallel to address unknown particles.

Methods

Aqueous electrolyte solutions were composed of 100 mM potassium chloride (Fluka) with 10 mM TRIZMA base (Sigma), buffered to pH 10 with KOH (Mallinckrodt), and were prepared using double-distilled water filtered through cellulose nitrate filter membranes (Nalgene, 200 nm pore size). Unless otherwise noted, all chemicals were used as received. After the addition of salts and buffering, electrolyte solutions were filtered twice more using polycarbonate filter membranes (Steriltech Corporation, 100 nm pore size). Solutions containing 50 nm and 100 nm silica nanoparticle (Polysciences, Inc.; size verified by SEM) were prepared by the serial dilution of the stock suspension ($\sim 10^{14}$ particles/ml for 50 nm particles and $\sim 10^{13}$ particles/ml for 100 nm particles) into the filtered

electrolyte until the desired bead concentration was reached ($10^9 - 5 \times 10^{10}$ particles/ml for this report). To prevent aggregation of the silica beads, suspensions were sonicated for 2 minute following the addition of the beads, then gently agitated overnight using a rotary mixer and finally sonicated again for 1 minute immediately before use. Nanoparticle samples used for zeta potential measurements were prepared in the same manner. A Malvern Zetasizer Nano ZS90 was used to determine zeta potentials using electrophoretic light scattering (ELS). A nanoparticle suspension is loaded into a clear U-shaped, cell with electrodes at either end. A voltage is applied to drive particles through a laser passing through the cell into a photodetector. Fluctuations in the intensity of the laser light that reaches the detector can be used to determine the electrophoretic mobility of the particles and is used to calculate their zeta potential.

Silicon nitride samples were furnished by Silson Ltd. (Northampton, UK) in the form of 5 mm x 5mm chips with three different membrane thicknesses: 50 nm, 100 nm and 500 nm. Nitride layers are grown via low pressure chemical vapor deposition (LPCVD) on both sides of a silicon support wafer. Using standard photolithographic techniques followed by plasma etching, a small portion of one of the nitride layers is removed. The exposed silicon is then etched with KOH, leaving a free-standing silicon nitride membrane. In this study, the membrane section accounted for an area of roughly $100 \mu\text{m} \times 100 \mu\text{m}$ on the chip.

Nanopores were milled in the free-standing membranes using a focused ion beam (FIB). Prior to milling, the membranes were coated with a thin (~ 10 nm) layer of metal to prevent accumulation of charge during ion milling and electron imaging. Two different instruments were employed for this study: an FEI Nova Dual Beam System (Lawrence Livermore National Lab) and a Zeiss 1540xB Cross Beam System (Lawrence Berkeley National Lab). The systems consist of two beams: an ion beam for milling (gallium ions are accelerated to 30 keV to ablate a target with nanoscale precision) and an electron beam for imaging; thus, a pore could be drilled and imaged/measured immediately afterwards. The

choice of instrument used was determined solely by availability. Through the preparation of several pores, milling parameters (ion beam current, spot size, mill depth and exposure time) were established to fabricate pores with diameters between 50 and 600 nm to within $\pm 10\%$ for both instruments; however, for this report, we focused on diameters in the range of roughly 200 nm -300 nm.

Gold was removed from the chips using Gold Etch Type TFA (Transene Company, Inc.), each was cleaned twice in a room temperature solution of freshly prepared piranha solution consisting of 3:1 v:v 98% sulfuric acid (Fisher):30% hydrogen peroxide (BHD) for at least 4 hours per cleaning and rinsed thoroughly after each cleaning with warm DI water. Please note that extreme care should be taken when working with piranha solution as it reacts explosively on contact with most organics. Chips were dried under nitrogen before being loaded into a custom polydimethylsiloxane (PDMS; Dow-Corning Sylgard 184) conductivity cell, which consisted of two compartments each containing a microfluidic channel.

When assembled, the pore represents the only connecting path between the two compartments/channels, *i.e.* any fluid or ion flow between the chambers is through the nanopore. The entire PMDS/silicon nitride assembly was exposed to an air plasma at low power (Harrick PDC-001 at 7 W) for 30 s to facilitate wetting of the cell and pore before filling with 100 mM KCl, 10 mM TRIS (pH 10.0). Using a HEKA EPC-10 patch clamp amplifier and Ag/AgCl pellet electrodes (A-M Systems) placed on both sides of the membrane, a voltage was sourced across the membrane while simultaneously measuring the ionic current through the pore. Currents were recorded for voltages between -100 mV and 100 mV in 10 mV increments in both increasing and decreasing directions to ensure there was no hysteresis. All measurements were performed inside a dark Faraday cage (Warner Instruments) on a vibration isolation table (Kinetic Systems, Inc.) to minimize electromagnetic and mechanical interference. As expected, all pores measured in this study displayed linear I-V curves. Using Eq. 4, we

could calculate a pore diameter based on its measured resistance and compare this value to the diameter determined using SEM measurements.

Upon successful verification of the pore diameter, the electrolyte in one chamber was replaced with a suspension of silica nanoparticles prepared as described above. The patch clamp amplifier was used to provide a constant voltage across the membrane while continuously monitoring the current in time. Using on-board electronics, the analog signal was filtered with a 10 kHz low-pass Bessel filter and digitized at 100 kHz. Bead translocation events were detected using software written in MATLAB (*The Mathworks*, R2010a; detection software by K. Healy). Briefly, the software scans the current traces, calculating mean values and standard deviations of the ionic current, and identifies an event when the current level falls below a user-defined number of standard deviations below the mean current. For detection purposes, this value was set between 4 and 5 (depending on the bead size, membrane thickness, pore diameter, *etc.*), but only those events that reached depths greater than 6 times the root mean square noise of an event-free interval (typical intervals were on the order of seconds, *i.e.* >> event durations) were included for analysis. This factor was chosen to ensure that the most intense fluctuations in the current *not* due to a bead passage would be disregarded. Additionally, only events lasting longer than twice the rise time of the low-pass filter were included for analysis because shorter duration events may be distorted by the filter. The rise time is roughly 1/3 of the inverse of the filter's cutoff frequency - 10 kHz in this case - so all events less than $\sim 70 \mu\text{s}$ were disregarded.

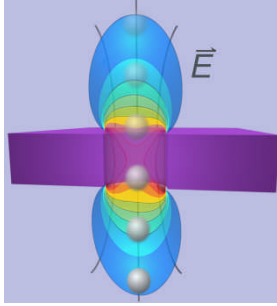
All histogram construction and curve fitting was performed with *Mathematica* (*Wolfram*, v8). For event durations, *Mathematica* was also used to determine the goodness of fit for lognormal and inverse Gaussian distributions using the Cramér-von Mises and Anderson-Darling tests. Referring to Eqs. 16 and 17, a and s parameters are calculated from considering all event duration data from an experiment and then substituting these values into appropriate equations. The resulting probability distribution is then compared to each individual data point and results are tabulated to evaluate the

likelihood of the distribution describing the experiment. When a test returns a statistical significance, *i.e.* the probability that the data matches the PDF purely by chance, of less than 5% for a given PDF, the hypothesis that the data is distributed according to that PDF is not rejected. Out of 122 tests - 61 for both the Cramér-von Mises and Anderson-Darling tests - 78 were not rejected for inverse Gaussian distributions (63.9%), while 79 were not rejected when compared to lognormal distributions (64.8%). Electric field distributions were calculated by numerically solving Poisson's equation for an insulating membrane using COMSOL v4.2.

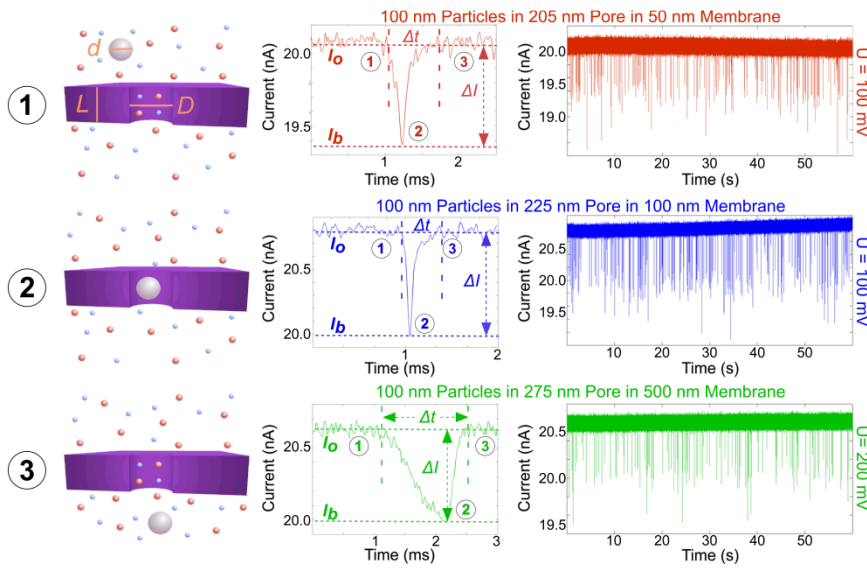
Acknowledgements

This work was performed under the auspices of the U.S. Department of Energy by Lawrence Livermore National Laboratory under Contract DE-AC52-07NA27344. This research was supported by the University of California Laboratory Fees Research Grant. Portions of this work (pore fabrication) were performed as a User project at the Molecular Foundry, Lawrence Berkeley National Laboratory, which is supported by the Office of Science, Office of Basic Energy Sciences, of the U.S. Department of Energy under Contract No. DE-AC02—05CH11231. M. Davenport wishes to acknowledge the financial support of the Lawrence Scholars Program and the Achievement Rewards for College Scientists Foundation. We acknowledge valuable discussions with Martin Langecker.

Figures:



TOC Image



Scheme 1:

(1) As a particle of diameter d approaches a pore, described by its own diameter D and length L , the current begins to drop from its baseline, open value, I_o , to a blocked value, I_b (2). The magnitude of the difference between these levels, ΔI , is recorded along with the duration of the translocation events – that is the time it takes for the particle to pass through the pore and the current to return to I_o (3). Several hundred such events are collected during a typical scan so that distributions for both event magnitudes and durations can be statistically analyzed.

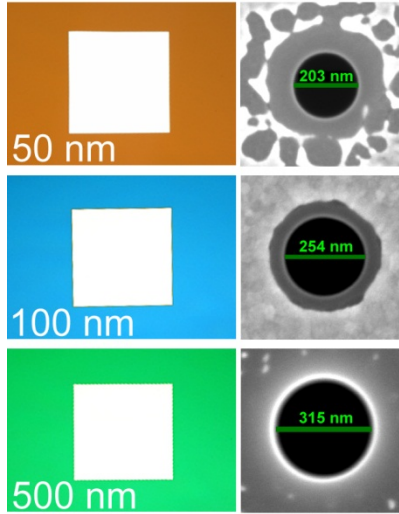


Figure 1: *Left* Optical microscope images of the free-standing silicon nitride membranes which appear as bright squares. The surrounding colored regions are caused by the thin-film interference of the nitride layer on the silicon support. Note that the colors of the membrane will be employed in a color-coding scheme for forthcoming plots: data pertaining to 50 nm membranes will be shown in red, 100 nm membranes in blue and 500 nm membranes in green. *Right* SEM micrographs of nanopores representing the range of pore diameters studied.

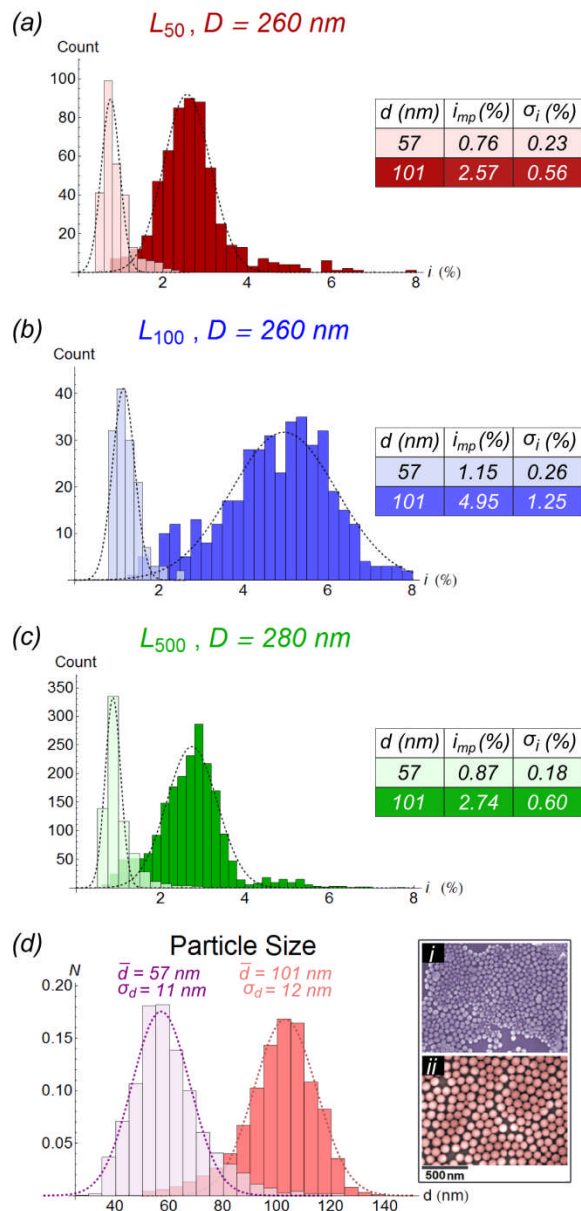


Figure 2: (a)-(c) Histograms showing event depth distributions for each membrane thickness. Note the similarities in shape between event depth and particle size distributions shown in (d). Particles were measured using an SEM; representative micrographs for 50 nm and 100 nm beads are shown in inset (i) and (ii) respectively (micrographs are false colored to match histograms).

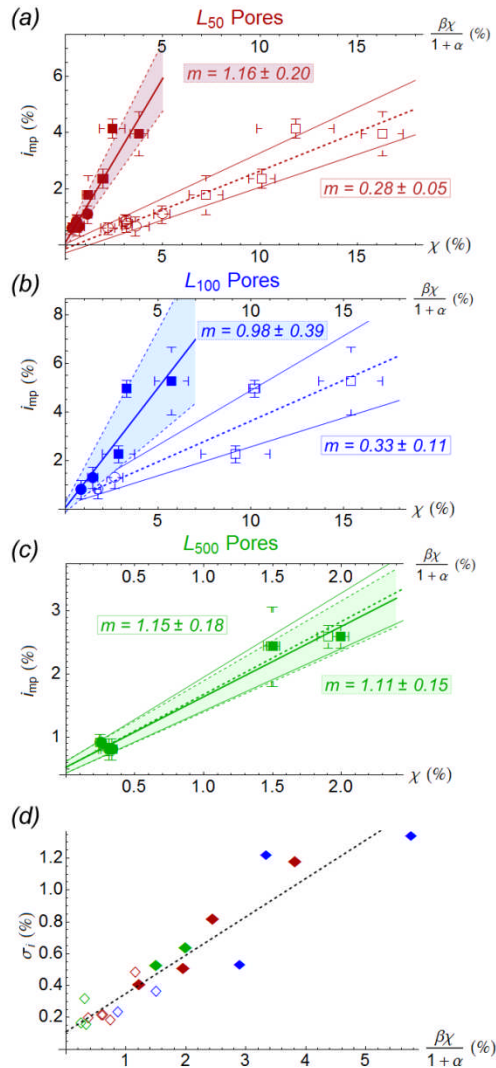
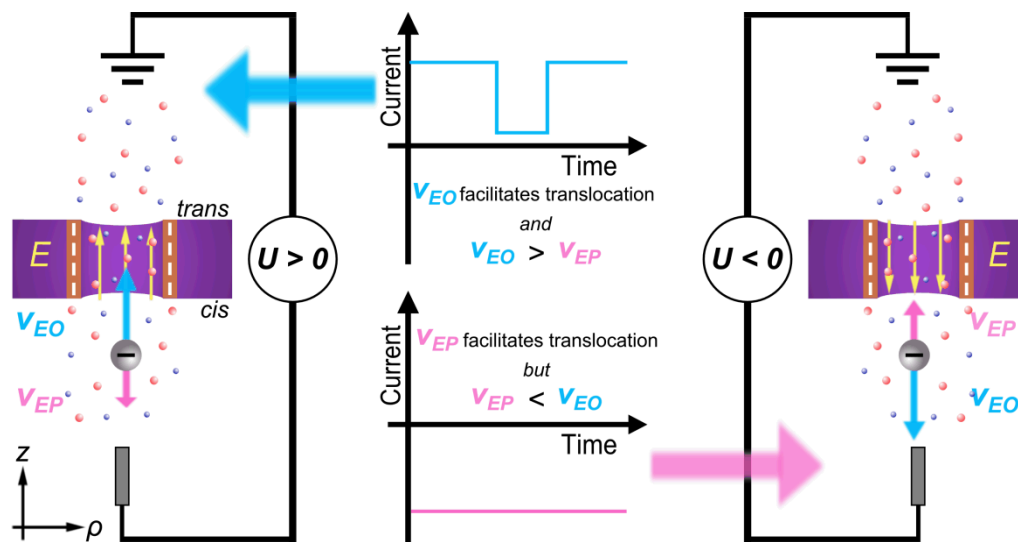


Figure 3 (a)-(c) Most probable i values are plotted for each membrane thickness versus the excluded volume, χ (empty markers), and $\beta \chi/(1+\alpha)$ (filled markers). Circles represent data collected for d_{50} particles and d_{100} experiments are shown as squares. Best fit lines are plotted for each case and bounded by lines accounting for uncertainties in the slope value. For excluded volume alone, the best fit line is dashed and the bounding lines and the area between is white. For $\beta\chi/(1+\alpha)$, the best fit line is solid and the bounding lines are dashed with the area between filled with the color corresponding to the membrane thickness. Abscissa values are determined by averaging SEM and electrochemical sizing of D ; the error bars are a reflection of the uncertainty in D . (d) Standard deviation versus $\beta\chi/(1+\alpha)$ is also found to be linear, supporting both the idea that our model is an improvement to event depth prediction and that the large standard deviations are related to the broad range of particle sizes. Empty diamonds represent d_{50} results and filled points are shown for d_{100} .



Scheme 2: When the applied voltage is positive, the electric field points from the *cis* to the *trans* side of the membrane. As the particle is negatively charged, its electrophoretic velocity, v_{EP} , frustrates translocation, but the electro-osmotic velocity resulting from the negative surface charge of the pore, v_{EO} , is sufficient to overcome v_{EP} and the particle moves through the pore. When the polarity reverses, so does the direction of the electric field and v_{EO} suppresses translocation. In this study, we have considered motion to be in the z -direction alone.

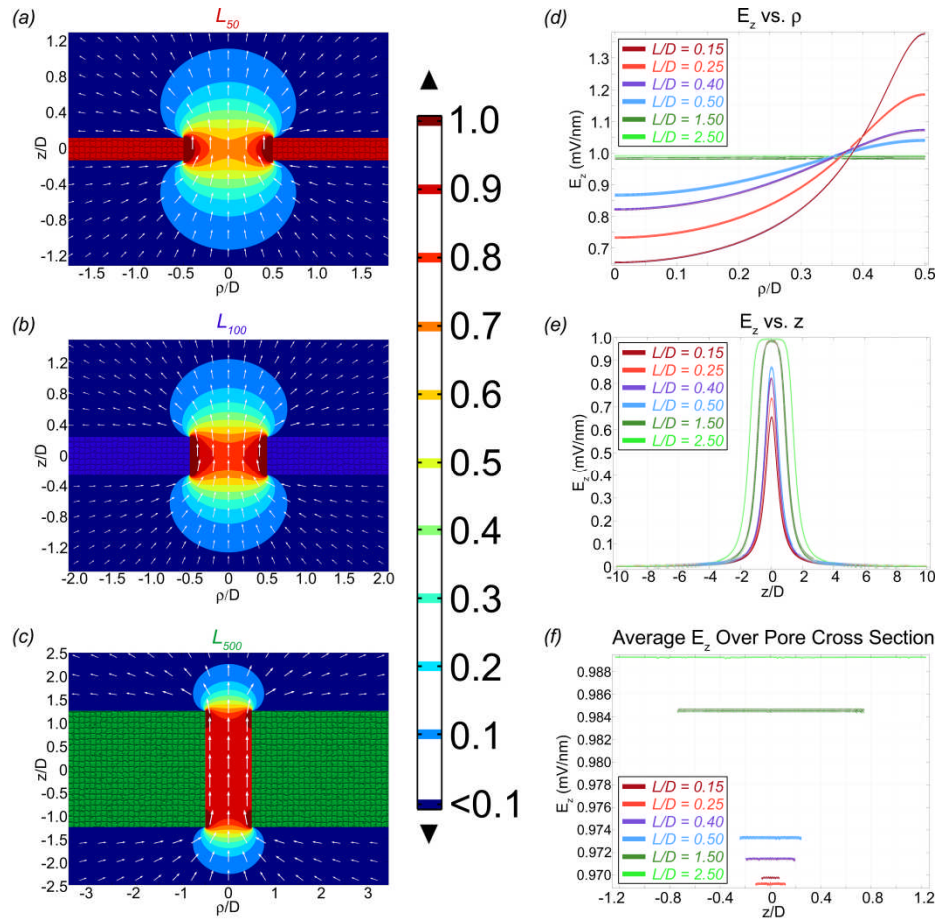


Figure 4: (a)-(c) Finite element analysis calculations for the z-component of the electric field, E_z , are shown as contours for the three membrane thicknesses. Membranes are textured and colored for easy identification. White arrows indicate the direction of the field. The voltage is $U = L + \pi D/4$ mV for facile comparison to Eq. 15. A field magnitude of 1 mV/nm represents regions where our approximation is most valid. The variation of the electric field strength is shown (d) over the radial direction, ρ , scaled in terms of pore diameter along the $z = 0$ radial line and (e) in the z-direction at $\rho = 0$. Note that the origin is taken to be the center of the pore. Our approximation is most valid for higher aspect ratio pores; however, in figure (f) we see that the average value E_z over the circular cross-sections of the pore is very nearly 1 mV/nm.

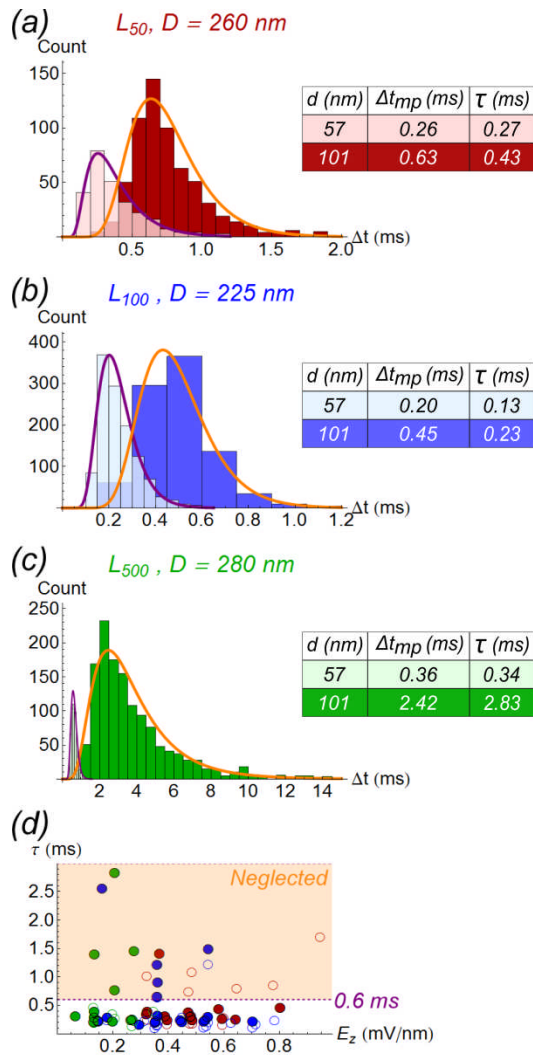


Figure 5: (a)-(c) Translocation times shown for the three membrane thicknesses at $E_z \approx 0.3 \text{ mV/nm}$. Inverse Gaussian fits are shown in purple for the d_{50} particles and lognormal curves are orange for the d_{100} particles. However, each particle size is fit with both PDFs and the resulting Δt_{mp} and τ values are averaged. Note the x-values of the L_{500} plot compared to the other histograms; long τ s are believed to be caused by poorly defined zeta potentials of either the pore or the particles (or both) or by non-specific interactions. For this reason, experiments with $\tau > 0.6 \text{ ms}$ were neglected as shown in (d).

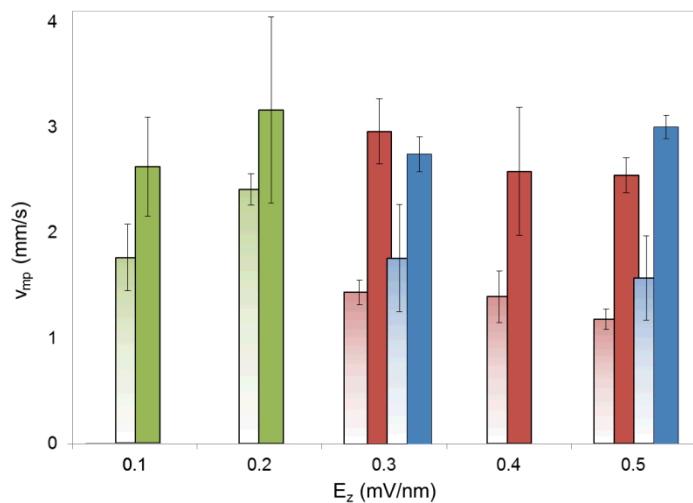


Figure 6: Velocities are averaged over E_z bin sizes of 0.1 mV/nm and shown for d_{50} (solid bars) and d_{100} experiments (gradient filling). Despite the large uncertainty, we can still determine that d_{100} particles translocate significantly slower than the d_{50} particles and calculate ζ_{particle} values that agree with ELS measurements. Interestingly, there is no discernible trend in particle velocity with either E_z or membrane thickness.

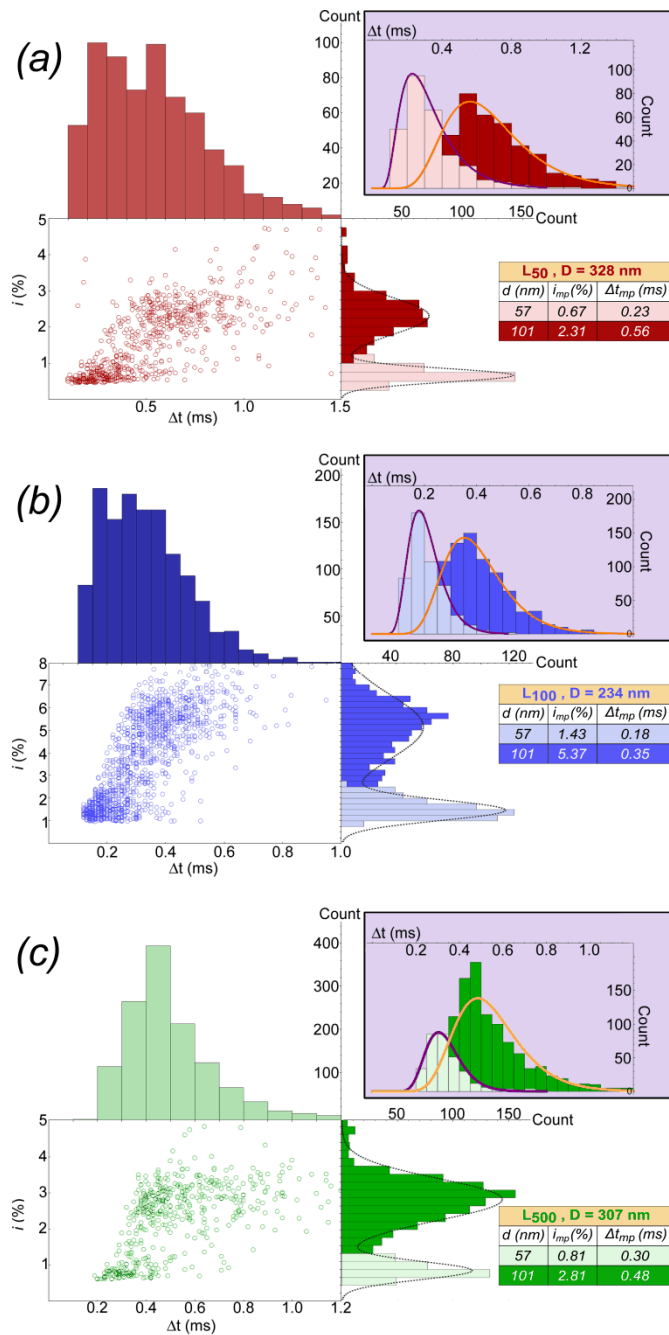


Figure 7: (a)-(c) show the results for experiments with mixtures of both particle sizes in L₅₀, L₁₀₀, and L₅₀₀ membranes respectively. The lower left hand side of each panel plots points according to their amplitude versus duration. To the right of this, the histograms for event depth are shown along with a fitting (dashed black line) that is the sum of two Gaussians. From the point of intersection of these Gaussian curves, we can divide the events into two categories: shallow and deep. Above the scatter is

the event duration histogram for all events; inset to the right of those are histograms showing event durations after the events are sorted according to depth. The shallow events are fitted with an inverse Gaussian curve (purple) and the deep events are shown with their corresponding lognormal fit (orange). The table is included to show both the mean event depth and most probable event duration (which is the average of the most probable times obtained from both the inverse Gaussian and lognormal fittings).

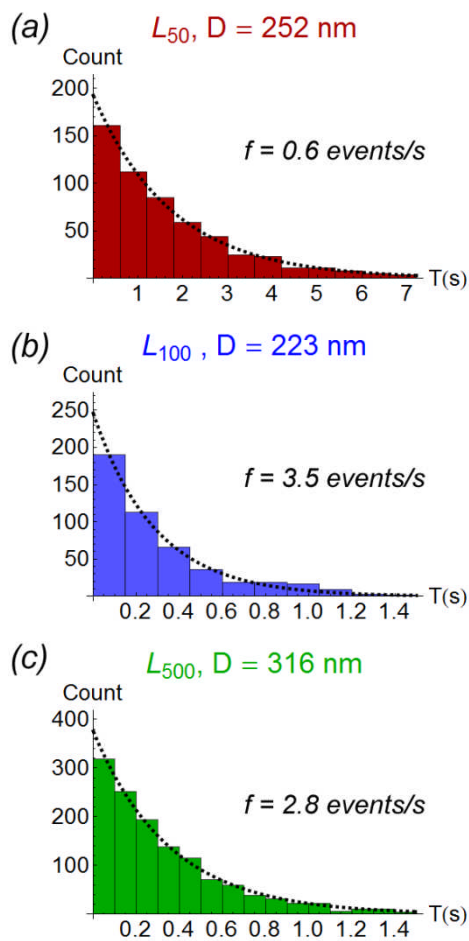


Figure 8: Distributions for the time between successive events, T , are plotted for the three membrane thicknesses. Each experiment shown was performed at $\xi \approx 0.15 \text{ Hz/mV}$ using d_{100} particles. f is determined by fitting histograms with an exponential decay $\sim e^{-fT}$.

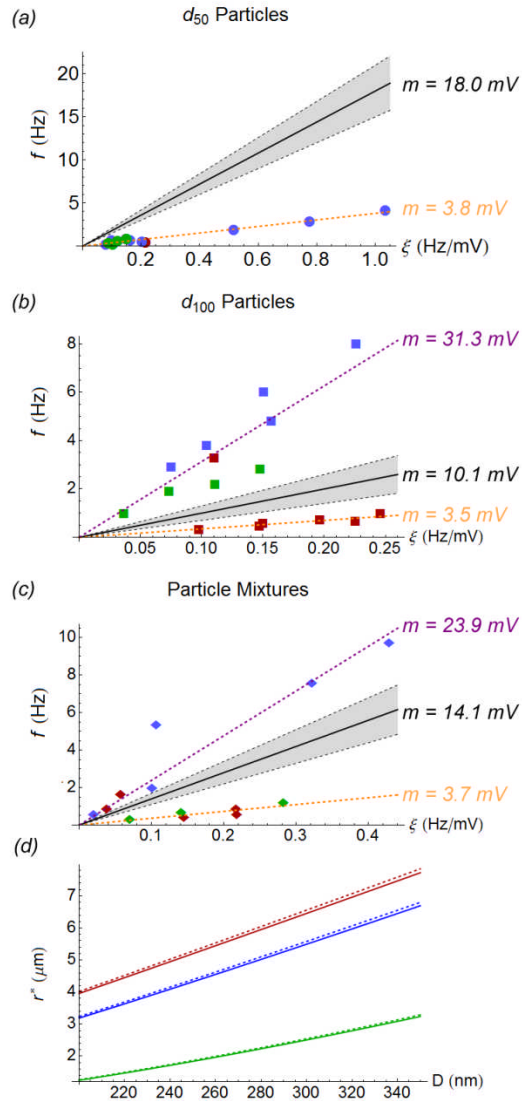


Figure 9: (a)-(c) Capture rate, f , is plotted for d_{50} and d_{100} particles, along with mixture of the two. Black lines represent $|\zeta_{\text{pore}}| - |\zeta_{\text{particle}}|$ according to $\zeta_{\text{pore}} = -44$ mV and ζ_{particle} determined from ELS data. For the mixture, event frequency scales as $\frac{C_{d50}}{C_{\text{tot}}} f_{50} + \frac{C_{d100}}{C_{\text{tot}}} f_{100}$, where C_s represent the concentration of the particles in the mixture. As $C_{d50} = C_{d100} = C_{\text{tot}}/2$, the slope of the theoretical line is given by $(2|\zeta_{\text{pore}}| - (|\zeta_{d50}| - |\zeta_{d100}|))/2$. Slope values are shown for the best fit line with a y-intercept of 0. There are clearly high and low capture rate regimes for 100 nm particles and the mixtures, with all of the L_{100} experiments belonging to the high frequency regime. Beyond that, it is unclear if there are any signs of capture rate dependence on pore length. We also show the capture radius, r^* , for the three membranes as a

function of pore diameter in (*d*). Dashed lines are for d_{50} particles and solid lines are for d_{100} beads. The lines for the different sized particles nearly overlap as $\delta_{d_{50}}/\delta_{d_{100}} \approx (|\zeta_{\text{pore}}| - |\zeta_{d_{100}}|)/(|\zeta_{\text{pore}}| - |\zeta_{d_{50}}|)$. Because *f* scales linearly with r^* , this plot suggests that thinner pores have higher capture rates, but we do not see this in our experiments.

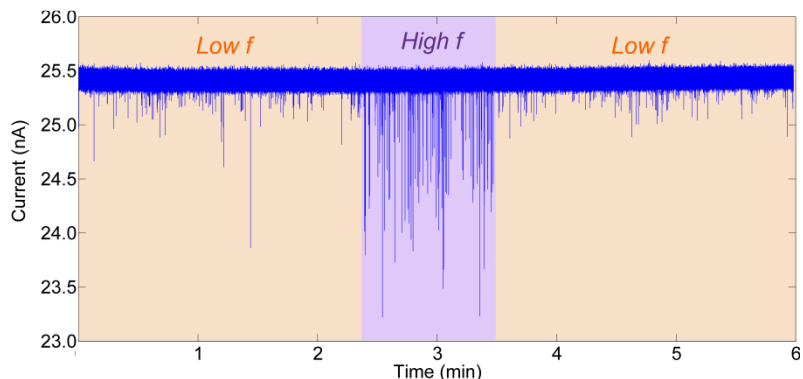


Figure 10: A mixture of 2×10^{10} d_{50} and d_{100} particles/ml (10^{10} /ml each) in a $D = 215$ nm, L_{100} pore at 150 mV. Within one six minute experiment, both low and high capture rates are demonstrated. In the low frequency portions, the events are primarily due to d_{50} particles, whereas many more d_{100} (deeper) events are seen in the high frequency section. While this indicates that *f* is intimately tied to the particle being detected, it is unclear exactly how particle parameters contribute to event frequency at this point.

¹ Bayley, H.; Martin, C.R. Resistive-Pulse Sensing – From Microbes to Molecules, *Chem. Rev.*, **2000**, *100*, 2575-2594

² Venkatesan, B.M.; Bashir, R. Nanopore Sensors for Nucleic Acid Analysis, *Nature Nanotech.*, **2011**, *6*, 615-624

³ Kasianowicz, J.J.; Brandin, E.; Branton, D.; Deamer, D.W. Characterization of Individual Polynucleotide Molecules Using a Membrane Channel, *Proc. Natl. Acad. Sci. USA*, **1996**, *93*, 13770-13773

⁴ Manrao, E.A.; Derrington, I.M.; Laszlo, A.H.; Langford, K.W.; Hopper, M.K.; Gillgren, N.; Pavlenok, M.; Niederweis, M.; Gundlach, J.H.; Reading DNA at Single-Nucleotide Resolution with a Mutant MspA Nanopore and Phi29 DNA Polymerase, *Nature Biotech.*, **2012**, *30*, 349-353

⁵ Cherf, G.M.; Lieberman, K.R.; Rashid, H.; Lam, C.E.; Karplus, K.; Akeson, M. Automated Forward and Reverse Ratcheting of DNA in a Nanopore at 5-Å precision, *Nature Biotech.*, **2012**, *30*, 344-348

⁶ Dekker, C. Solid-State Nanopores, *Nature Nanotech.*, **2007**, *2*, 209-215

⁷ Healy, K. Nanopore-Based Single-Molecule DNA Analysis: A Review, *Nanomedicine*, **2007**, *2*, 459-481

⁸ Healy, K.; Schiedt, B.; Morrison, A.P.; Solid State Nanopore Technologies for Nanopore-Based DNA Analysis, *Nanomedicine*, **2007**, *2*, 875-897

⁹ Branton, D.; Deamer, D.W.; Marziali, A.; Bayley, H.; Benner, S.A.; Butler, T.; Di Ventra, M.; Garaj, S.; Hibbs, A.; Huang, X. *et al*, The Potential and Challenges of Nanopore Sequencing, *Nature Biotech.*, **2008**, *26*, 1146-1153

¹⁰ Wanunu, M. Nanopores: A Journey Towards DNA Sequencing, *Phys. Life Rev.*, **2012**, *9*, 125-158

¹¹ Coulter, W.H.; Means for Counting Particles Suspended in a Fluid. *US Patent No. 2656508*, **1953**

-
- ¹² Han, A.; Schürmann, G.; Mondin, G.; Bitterli, R.A.; Hegelbach, N.G; de Rooij, N.F.; Staufer, U. Sensing Protein Molecules Using Nanofabricated Pores, *Appl. Phys. Lett.*, **2006**, *88*, 093901
- ¹³ Skinner, G.M.; van den Hout, M.; Broekmans, O.; Dekker, C.; Dekker, N.H.; Distinguishing Single- and Double-Stranded Nucleic Acid Molecules Using Solid-State Nanopores, *Nano Lett.*, **2009**, *9*
- ¹⁴ DeBlois, R.W.; Bean, C.P.; Wesley, R.K.A. Electrokinetic Measurements with Submicron Particles and Pores by the Resistive Pulse Technique, *J. Colloid Interface Sci.*, **1977**, *61*, 323-335
- ¹⁵ Pevarnik, M.; Healy, K.; Toimil-Molares, Morrison, A.; Létant, S.E.; Siwy, Z.S. Polystyrene Particles Reveal Pore Substructure as They Translocate, *Submitted*
- ¹⁶ DeBlois, R.W.; Bean, C.P. Counting and Sizing of Submicron Particles by the Resistive Pulse Technique. *Rev Sci Instr.* **1970**, *41*(7), 909-916
- ¹⁷ DeBlois, R.W.; Wesley, R.K.A. Sizes and Concentrations of Several Type C Oncornaviruses and Bacteriophage T2 by the Resistive-Pulse Technique. **1977**, *23* (2), 227-233
- ¹⁸ Uram, J.D.; Ke, K.; Hunt, A.J.; Mayer, M. Submicrometer Pore-Based Characterization and Quantification of Antibody-Virus Interactions, *Small*, **2006**, *2*, 967-972
- ¹⁹ Lan, W.-J.; Holden, A.D.; Zhang, B.; White, H.S. Nanoparticle Transport in Conical-Shaped Nanopores, *Anal. Chem.* **2011**, *83*, 3840-3847
- ²⁰ Lan, W.-J.; Holden, D.A.; Liu, J.; White, H.S. Pressure-Driven Nanoparticle Transport across Glass, *J. Phys. Chem. C*, **2011**, *115*, 18445-18452
- ²¹ Lan, W.-J.; White, H.S.; Diffusion Motion of a Particle Translocating through a Nanopore, *ACS Nano*, **2012**, *6*, 1757-1765
- ²² Zhou, K.; Li, L.; Tan, Z.; Zlotnick, A.; Jacobson, S.C. Characterization of Hepatitis B Virus Capsids by Resistive-Pulse Sensing, *J. Am. Chem. Soc.* **2011**, *133*, 1618-1621
- ²³ Sun, L.; Crooks, R.M. Fabrication and Characterization of Single Pores for Modeling Mass Transport across Porous Membranes, *Langmuir*, **1999**, *15*, 738-741
- ²⁴ Tsutsui, M.; Hongo, S.; Hem Y.; Taniguchi, M.; Gemma, N.; Kawai, T. Single-Nanoparticle Detection Using a Low-Aspect-Ratio Pore. *ACS Nano*, **2012**, *6*, 3499-3505
- ²⁵ Bacri, L.; Oukhaled, A.G.; Schiedt, B.; Patriarche, G.; Bourhis, E.; Gierak, J.; Pelta, J.; Auray, L. Dynamics of Colloids in Single Solid-State Nanopores. *J. Phys. Chem. B*, **2011**, *115*, 2890-2898
- ²⁶ Prabhu, A.S.; Jubery, T.Z.N.; Freedman, K.J.; Mulero, R.; Dutta, P.; Kim, M.J.I. Chemically Modified Solid State Nanopores for High Throughput Nanoparticle Separation, *J. Phys.: Condens. Matter*, **2010**, *22*, 454107-454115
- ²⁷ Saleh, O.A.; Sohn, L.L. Quantitative Sensing of Nanoscale Colloids Using a Microchip Coulter Counter, *Rev. Sci. Instr.*, **2001**, *72*, 4449-4451
- ²⁸ Sun, L.; Crooks, R.M.; Single Carbon Nanotube Membranes: A Well-Defined Model for Studying Mass Transport through Nanoporous Materials, *J. Am. Chem. Soc.*, **2000**, *122*, 12340-12345
- ²⁹ Ito, T.; Sun, L.; Crooks, R.M. Simultaneous Determination of the Size and Surface Charge of Individual Nanoparticles Using a Carbon Nanotube-Based Coulter Counter, *Anal. Chem.*, **2003**, *75*, 2399-2406
- ³⁰ Ito, T.; Sun, L.; Bevan, M.A.; Crooks, R.M. Comparison of Nanoparticle Size and Electrophoretic Mobility Measurements Using a Carbon-Nanotube-Based Coulter Counter, Dynamic Light Scattering, Transmission Electron Microscopy, and Phase Analysis Light Scattering, *Langmuir*, **2004**, *20*, 6940-6945
- ³¹ Petrossian, L.; Wilk, S.J.; Joshi, P.; Goodnick, S.M.; Thornton, T.J. Demonstration of Coulter Counting through a Cylindrical Solid State Nanopore, *J. Phys: Conf. Series*, **2008**, *109*, 012028-012031
- ³² Hall, J.E. Access Resistance of a Small Circular Pore, *J. Gen. Phys.*, **1975**, *66*, 531-532
- ³³ Gregg, E.C.; Steidley, K.D. Electrical Counting and Sizing of Mammalian Cells in Suspension. *Biophys J*, **1965**, *5*, 393-405
- ³⁴ Wanunu, M.; Sutin, J.; McNally, B.; Chow, A.; Meller, A.; DNA Translocation Governed by Interactions with Solid-State Nanopores. *Biophys. J.* **2008**, *95*, 4716-4725
- ³⁵ Wei, R.; Pedone, D.; Zürner, A.; Döblinger, M.; Rant, U. Fabrication of Metallized Nanopores in Silicon Nitride Membranes for Single-Molecule Sensing. *Small*. **2010**, *6*, 1406-1414
- ³⁶ Bousse, L.; Mostarshed, S. The Zeta Potential of Silicon Nitride Thin Films. *J. Electroanal. Chem.* **1991**, *302*, 269-274
- ³⁷ Schoch, R.B.; Han, J.; Renaud, P. Transport phenomena in nanofluidics. *Rev. Mod. Phys.* **2008**, *80*, 839-883

-
- ³⁸ Firnkes, M.; Pedone, D.; Knezevic, J.; Döblinger, M.; Rant, U. Electrically Facilitated Translocation of Proteins through Silicon Nitride Nanopores: Conjoint and Competitive Action of Diffusion, Electrophoresis, and Electroosmosis. *NanoLett.* **2010**, 2162-2167
- ³⁹ Yusko, E.C.; An, R.; Mayer, M.; Electroosmotic Flow Can Generate Ion Current Rectification in Nano- and Micropores. *ACS Nano.* **2010**, 4, 477-487
- ⁴⁰ Hall, A.R.; Keegstra, J.M.; Duch, M.C.; Hersam, M.C.; Dekker, C. Translocation of Single-Wall Carbon Nanotubes Through Solid-State Nanopores. *NanoLett.* **2011**, 11, 2446-2450
- ⁴¹ Soni, G.V.; Dekker, C. Detection of Nucleosomal Substructures using Solid-State Nanopores. *NanoLett.* **2012**, 12, 3180-3186
- ⁴² Tweedie, M.C.K. Inverse Statistical Variates, *Nature*, **1945**, 155, 453
- ⁴³ Wanunu, M.; Morrison, W.; Rabin, Y.; Grosberg, A.Y.; Meller, A. Electrostatic Focusing of Unlabelled DNA into Nanoscale Pores Using a Salt Gradient, *Nature Nanotech.*, **2010**, 5, 160 – 165 (Supplementary Information)
- ⁴⁴ Wong, C.T. and Muthukumar, M. Polymer Capture by Electro-Osmotic Flow of Oppositely Charged Nanopores, *J Chem. Phys.*, **2007**, 126, 164903-164908
- ⁴⁵ Nam, S.-W.; Rooks, M.J.; Kim, K.-B.; Rossnagle, S.M. Ionic Field Effect Transistors with Sub-10 nm Multiple Nanopores, *Nano. Lett.*, **2009**, 9, 2044-2048
- ⁴⁶ He, Y.; Tsutsui, M.; Fan, C.; Taniguchi, M.; Kawai, T. Gate Manipulation of DNA Capture into Nanopores. *ACS Nano*, **2011**, 10, 8391-8397